Resonant Vibrational Modes and Effective Damping Factor of a Rocket in Flight

Akhil Bagaria, Benjamin Chasnov, Richard Piersall, Apoorva Sharma

Harvey Mudd College

E80 | Section 3 Team 1

5 May 2014

Abstract—**The vibrational behavior of a rocket is critical to characterize, in order to design for structural stability under hazardous loading conditions. Thus, we used analytical modeling, finite element analysis, and real-world in-flight strain gauge data to characterize our rocket's transverse vibrational modes. Our flight data—recorded from launching an Aerotech Barracuda on a G79 motor—shows two distinct modes, corresponding to closely matching modes in our analytical and numerical models. The first indicates resonance with two nodes. This mode has a frequency of $37 \pm 11\,\text{Hz}$ in the analytical model, $28.319\,\text{Hz}$ in the SolidWorks model, and $40.4 \pm 1.3\,\text{Hz}$ in the flight data. The second indicates resonance with the same two nodes, plus a third one directly between them. This mode oscillates at $115 \pm 36\,\text{Hz}$ in the analytical model, $106.37\,\text{Hz}$ in the SolidWorks model, and $130.5 \pm 2.4\,\text{Hz}$ in the flight data. Each nodes frequencies fall within the range predicted by our analytical model.**

I. Introduction

Vibrational analysis plays a crucial role in rocketry. During flight, external forces excite vibrations in the rocket. Resonance induced in the rocket can have devastating effects if amplitudes of vibrations are not controlled. To prevent such problems, it is necessary to understand which resonant modes are excited in flight.

In this paper, we attempt to do just this. Using piezoelectric strain gauges and a pair of accelerometers, we experimented on an Aerotech Barracuda rocket and ran additional tests using a secondary, custom-built rocket (A note will be made anytime this secondary rocket is being referenced).

In order to predict the rocket's frequency response, we start by developing both an analytical and a numerical model for the rocket's oscillation. Following that, we discuss ground-based experimental techniques to determine the system's resonant modes and damping factor. Finally, we report the results from the rocket's flight and compare these results to the models. In all, this allows us to recommend certain design choices to minimize negative effects of resonant vibrations.

A. Background Info

As the rocket is forced through the air by burning fuel and buffeted by the passing air, it flexes and distorts. These forces excite all frequencies in the rocket, but at certain *resonant* frequencies, the input forces constructively interfere with existing vibrations. The rocket then tends to oscillate with much greater amplitude at those frequencies. The rocket can exhibit transverse (side to side), longitudinal (shortening and lengthening), dilatational (widening and narrowing), and torsional (twisting) oscillation, but we will focus here on transverse modes. In general, these vibration patterns are henceforth referred to as *resonant modes*.

In order to determine the resonant frequencies of an object, it is necessary to determine the frequency response. To do so, a system is stimulated with a range of frequencies and the resulting amplitude of oscillation is recorded. Two methods of supplying this stimulus are the tap test and the sweep test. In a tap test, the rocket is hit with an impulse hammer, a device which records the input signal via sensors in the hammerhead itself. This input approximates a Dirac Delta function, which has a uniform distribution of frequency components. In a sweep test, the rocket is stimulated with vibrations of varying input frequency. In both tests, the resonant frequencies of the rocket are excited by the corresponding stimuli, and by observing the system's oscillation in the frequency domain, peaks can be observed for each of those resonant modes.

Through loss of kinetic energy to the surroundings, the amplitude of these oscillations will decrease over time in a process known as damping. The higher the damping factor, the faster oscillations will weaken and disappear. Because damping can influence and shift resonant frequencies, changes in damping factor can alter how the rocket vibrates.

II. Experimental Design

In our experiment, we hoped to characterize the rocket in terms of the aforementioned parameters of resonant modes and damping.

A. Goals

The primary goal of this experiment was to determine the frequencies and shapes of the rocket's vibrational modes while in flight.

While identifying resonant frequencies informs important rocket design decisions, the frequencies and shapes alone do not give the full picture. The rocket like all real world systems, has inherent damping. We hypothesized that the rocket's damping factor would relate to its velocity, because as the rocket accelerates, added strain and pressure on the body might change system properties.

Our secondary goal was thus to investigate the relationship between the damping factor of the rocket and its velocity. More specifically, we wanted to study the damping factor at transonic velocities because the drastic difference between subsonic and supersonic flows would yield more interesting trends.

B. Sensor Selection

1) IMU: In order to determine the velocity of the rocket during flight, we used data from a Mudd IMU3 board. Of the two accelerometers and two gyroscopes on the IMU board, we recorded only the high-g accelerometer and the single low-g accelerometer along the same axis (board y axis, longitudinal axis of rocket). As our only independent variable of interest was the longitudinal velocity of the rocket, and the only part of our flight during which we anticipated useful data was the few seconds of acceleration by the rocket motor (during which the rocket would be approximately vertical), we chose to neglect the horizontal acceleration data from the rest of the low-g accelerometer and the rotation data from the gyroscopes. This also allowed us more datalogger channels for other sensors.

OpenRocket simulations for our rocket indicated a max acceleration of 17g's with a G79 motor and 31 g's with an H165 motor. For the AD22280 high-G accelerometer, both of these fall well within its range of $\pm$ 50g's. The output of this chip is a low-impedance, analog, DC voltage signal, ranging from 0 to 5V, centered at 2.5V and exhibiting a linear relationship to acceleration with slope 38 mV/g. Thus, for the H motor, the output voltage should range between $2.5\,\text{V}$ and $2.5 + 0.038 \cdot 31 = 3.68\,\text{V}$.
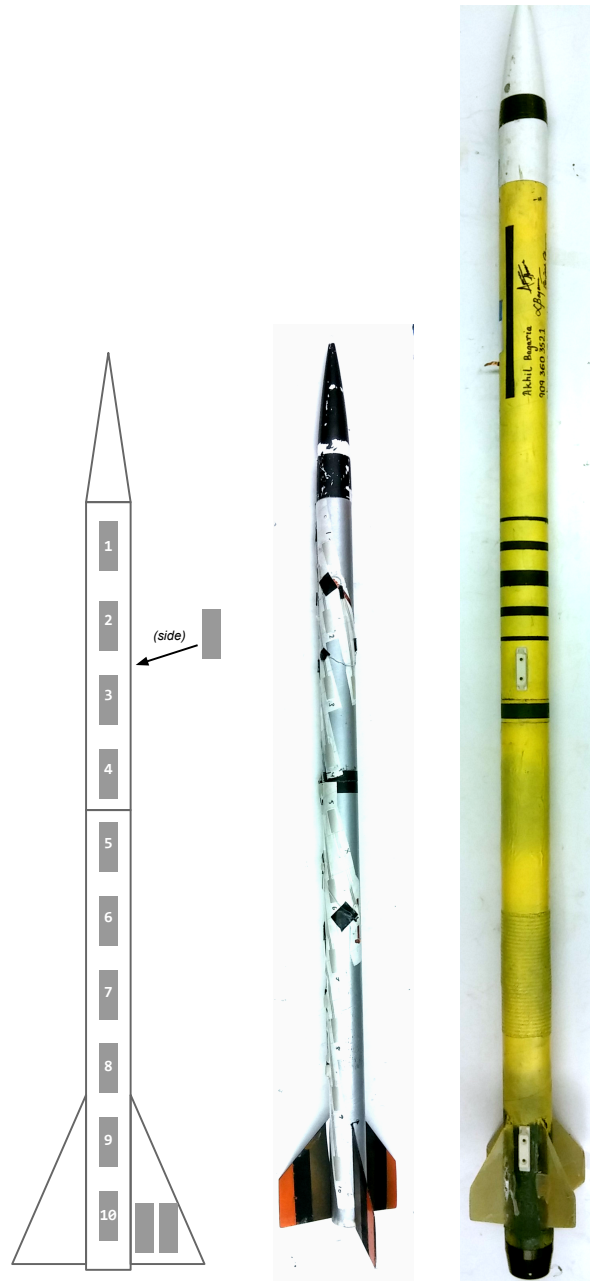

Fig. 1. *Left*: Placement of the 13 piezo strain gauges
Middle: Aerotech Barracuda, primary experimental platform
Right: Custom-built rocket, secondary experimental platform

The MMA7331L low-G accelerometer will be maxed out during this stage of the flight, as it has a maximum acceleration of 4 g's. However, it will still allow us to record the effects of gravity and drag after the rocket motor burns out. The output signal from this chip is also a low-impedance analog DC voltage, centered at 1.4 volts and increasing by 308 millivolts for each g of acceleration. Since negative acceleration due to drag and gravity shouldn't exceed two g's, the output voltage of this chip should range between 1.4 and 2 volts.

2) Piezoelectric Strain Gauges: In order to track vibrations along the rocket, we attached piezoelectric dynamic strain gauges to its surface. These gauges are cheaper and output at higher voltages than conventional strain gauges, which put less strain on our budget and circuitboard space.

Because these gauges are simply pieces of piezoelectric material, they have no maximum input value before the mechanical failure point. These devices each output a low-impedance, analog, AC voltage signal, proportional to vibrational amplitude and centered on zero volts.

C. Rocket Design

For our experimentation we constructed two entirely different rockets. The first was an Aerotech Barracuda, modified as prescribed for Mudd's E80 course (with a longer booster section and different motor retainer), and designed to fly on a G or H motor [1]. This rocket was outfitted with thirteen external piezoelectric strain gauges and painted to be aesthetically pleasing. See Figure 1 for a picture of this rocket.

The second was a custom rocket built from 54mm Apogee Blue Tube and intended to fly at subsonic speeds on an I motor or at transonic speeds on a J motor. The body material was chosen for its strength, and was assembled to be the minimum diameter capable of holding an I or J motor, to enable it to reach and survive supersonic flight. This rocket was outfitted with a single external piezoelectric strain gauge and also painted to be aesthetically pleasing. See Figure 1 for a picture.

From this point in the paper, all instances of the rocket will refer to the Aerotech Barracuda, unless otherwise specified.

D. Sensor and Actuator Design

We created a strain gauge array using thirteen MSI FDT1-028K strain gauges on the body of the rocket, attached directly to the body of the rocket with the included adhesive backing. As visible in Figure 2c, ten were arranged collinearly down the body of the rocket from tip to tail, four on the payload section and six on the booster section. We expected that this linear arrangement would allow us to see transverse oscillations far more clearly. An eleventh strain gauge, just visible in the same figure, was placed on the payload section, orthogonal to the line of ten gauges to give us a view of dilatational oscillation modes. The twelfth and thirteenth gauges, shown in Figure 2b, were placed on one of the rocket's fins to give us a better view of their oscillation.

(a) Automated tapper with solenoid head visible.

(b) Detail of strain gauges 12 and 13, mounted to a fin

(c) Strain gauges 1, 2, and 3. Gauge 11 (orthogonal gauge) is partially visible above gauge 2

Fig. 2. Close up photos of important sections of the rocket.

The z-axis accelerometers were mounted on the circuit board using standard 2.54mm header pins.

Note: Custom Rocket – An automated tapper device was designed to provide a continuous stream of impulse taps on the rocket body. These taps excite controlled transients along the rocket body, which were used to calculate the rocket's damping factor during flight. A small solenoid (ZHO-0420L/S) is momentarily triggered on by a 5ms pulse at 18V. These pulses are generated every 200ms by an arduino running on 3.3V logic. To eliminate the possibility of noise interference, the entire tapper assembly is electrically isolated from the logger board and encased in an fullbody aluminum and steel faraday cage. The assembled device is shown in Figure 2a.

E. Circuit Design

We powered our op-amps and the IMU with a single LM7805 5V regulator and two MCP1702-3302 3.3V regulators. The 5V regulator powers the IMU's 5V pin as well as each op-amp chip. One 3.3V regulator powers the 3.3V pin on the IMU, while the other provides one input of the floating ground circuit. The power supply schematics are shown in Figure 3.

Using just two of the IMU's outputs, we only needed to connect to seven of its 20 pins. Pins 2-1 and 1-2 are grounded, pins 1-10 and 2-8 are connected to the first

3.3V regulator, and pin 1-1 is connected to the 5V rail. The only outputs of interest come from pins 1-4 and 1-6.

Since both accelerometers and all of the piezos have low output impedance and the datalogger has a low input impedance, all signals were routed through high-impedance op-amps. Otherwise, the sensors may have formed unintended voltage dividers and given us incorrect data.

The output of the low-g accelerometer is already in the same range as the datalogger, but the high-g accelerometer can go as high as 5V. We scaled this down to 0–3V with a voltage divider. Both signals are then stabilized and buffered with unity gain op-amps. The High-G accel circuit is shown in Figure 4a, while the Low-G accel circuit is in Figure 4b.

The strain gauges output a signal that is centered on zero, so we needed an offset to center it in the datalogger's input range. We used a voltage divider to halve 3.3V to 1.65V and stabilized it with a unity gain op-amp, as seen in Figure 4c. Buffering capacitors further stabilize the output.

To condition the output of each strain gauge, we used thirteen identical copies of the circuit shown in Figure 4d. The 1.65V floating ground brings the signal into a readable range. The unity gain op-amp then stabilizes the signal and gives it a high output impedance before it is routed to the datalogger.

For the datalogger, we assumed that the frequencies that would be aliased — those at and above the nyquist frequency of $(100000/16)/2 = 3200\,\mathrm{hz}$ — wouldn't exist in the rocket. Thus, we simply left our signals unfiltered and selected the maximum possible sampling frequency. In retrospect, after seeing that our data did indeed include aliased frequencies, we realized that we should have included an analog filter.

Note: Custom Rocket – After seeing the aliased signals in our data from the first flight, we added a hardware filter to the circuitry for our custom rocket. In our testing of the rocket, we found that the frequencies of interest would be between 20 and 600 Hz. Thus, in order to eliminate frequencies much higher than that (especially those above 3200 Hz), we built a Sallen-Key topology, 3rd order Bessel Filter with the specifications shown in Figure 5, giving a cutoff frequency of about 2000 Hz [2].
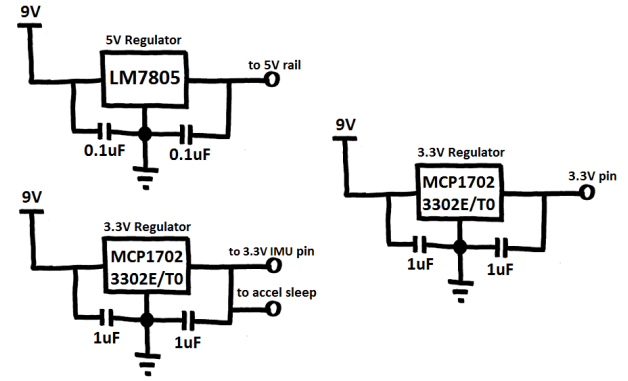
Fig. 3. Power supplies for circuitboard. Buffering capacitors reduce power supply noise for all three. Third supply leads to floating-ground circuit.
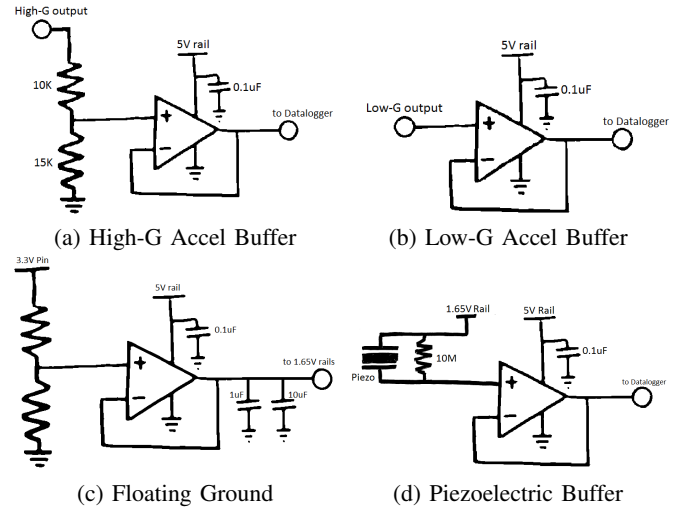
(a) High-G Accel Buffer

(b) Low-G Accel Buffer

(c) Floating Ground

(d) Piezoelectric Buffer

Fig. 4. Signal Conditioning Circuitry using MCP6004 Low-power Op-Amps

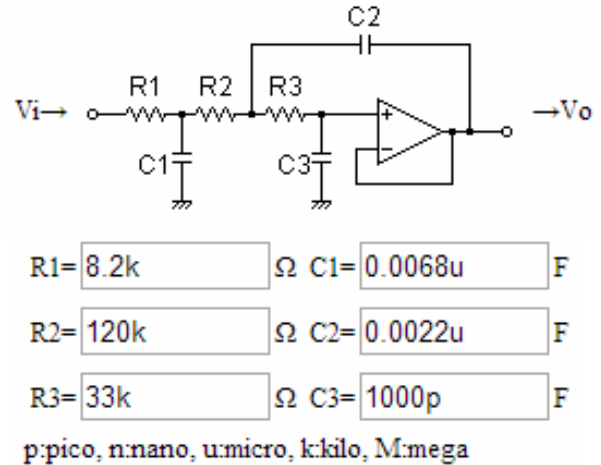|		
R1= 8.2k	Ω	C1= 0.0068u	F
R2= 120k	Ω	C2= 0.0022u	F
R3= 33k	Ω	C3= 1000p	F

p:pico, n:nano, u:micro, k:kilo, M:mega

Fig. 5. Filter Specs. 3rd Order Bessel Filter, Sallen-Key topology.

III. ANALYTICAL MODEL OF ROCKET

Before running experiments using the hardware described above, we developed an analytical model of the rocket. In this section, we discuss the development of such an analytical model. We had two goals in mind while developing this analytical model. First, we wanted to be able to predict the resonant frequencies of our rocket with the help of the Euler-Bernoulli Beam Theory [3]. Second, we wanted to validate the results obtained from the SolidWorks finite element simulation discussed in section IV and the results obtained from the conducted ground tests discussed in sections VI-A and VI-B.

We model our rocket as a free-free beam having uniform density and no damping. First, we derive the governing equation that describes the dynamics of a homogenous, uniform density beam. Then in subsection III-B, we derive the resonant frequencies and corresponding mode shapes for a simple free-free beam. The free-free beam analysis is followed by an analysis os a more sophisticated model of a free-free beam with a point mass addition on one end. This section ends with a list of resonant frequencies and mode shapes as predicted by such a model in subsection III-C.

A. Derivation of the Dynamic Beam Equation

The model's physical structure is shown in Figure 6.

Let S denote the energy function associated with a beam under dynamic loading conditions, defined as:

$$S = \int_0^L \left[\frac{1}{2}\mu(\frac{\partial y}{\partial t})^2 - \frac{1}{2}EI(\frac{\partial^2 y}{\partial x^2})^2 + q(x)y(x,t) \right] dx \tag{1}$$

where E is the Young's Modulus, and I is the second moment of inertia.

In equation 1, the first term represents the kinetic energy where μ is the mass per unit length; the second term represents the potential energy due to internal forces and the third term represents the potential energy due to the external load $q(x)$.

The Euler-Lagrange equation is then used to determine the function that minimizes the energy function S [4][5]. For a dynamic beam, the Euler-Lagrange equation is

$$\frac{\partial^2}{\partial x^2}(EI\frac{\partial^2 y}{\partial x^2}) = -\mu\frac{\partial^2 y}{\partial t^2} + q(x)$$

where, A is the area of cross section, and ρ is the (uniform) density of the beam.

We assume that the beam is homogenous, which implies that E and I are independent of x. We also assume free-response vibrations of the beam which implies that $q(x) = 0$. The governing equation for the free vibrations of a homogenous beam having uniform density thus gets reduced to:

$$EI\frac{\partial^4 y}{\partial x^4} + \rho A\frac{\partial^2 y}{\partial t^2} = 0$$

This governing equation may be re-written as

$$\frac{\partial^2 y(x,t)}{\partial t^2} + \frac{EI}{\rho A}\frac{\partial^4 y(x,t)}{\partial x^4} = 0 \tag{2}$$

The solution of the above governing equation is a standing wave which may be written as:

$$y(x,t) = w(x)u(t) \tag{3}$$

The governing equation also leads to the following relation for angular frequency:

$$\omega_i = (\beta_i L)^2 \sqrt{\frac{EI}{\rho A L^4}} \tag{4}$$

Note that the term $\beta_i L$ is known as the ith normalized frequency of the system. The rest of this subsection, as well as the next, is devoted to deriving the normalized resonant frequencies of the system in question. These normalized resonant frequencies are independent of the specific characteristics of the beam (E, I, ρ, A).

After deriving the general normalized resonant frequencies, we derive the actual resonant frequencies for our rocket by plugging in values for E, I, ρ, and A.

Substituting this standing wave equation (3)) into (2) yields the following result:

$$\frac{1}{u(t)}\frac{\partial^2 u(t)}{\partial t^2} = -\frac{EI}{\rho A}\frac{1}{w(x)}\frac{\partial^4 w}{\partial x^4} \tag{5}$$

Since the left side of (5) is a function of time only and the right side of the equation is a function of space only, and the two sides are equal for all x and t, both sides must be equal to a constant. This constant will be arbitrarily denoted as $-\omega^2$ The spatial portion of (5) can thus be written as:

$$\frac{\partial^4 w(x)}{\partial x^4} = \frac{\rho A \omega^2}{EI}w(x)$$

The spatial differential equation has the general solution:

$$w(x) = C_1 \sin\beta x + C_2 \cos\beta x$$
$$+ C_3 \sinh\beta x + C_4 \cosh\beta x \tag{6}$$

B. Free-Free Beam Model

Now, we apply boundary conditions to the left side of the free-free beam.

The no moment boundary condition implies

$$w''(0) = 0$$

$$\implies -C_2 + C_4 = 0 \qquad (7)$$

The no shear boundary condition implies

$$w'''(0) = 0$$

$$\implies -C_1 + C_3 = 0 \qquad (8)$$

Now we apply boundary conditions to the right side of the beam. The no force boundary condition implies that

$$w''(L) = 0$$

$$\begin{aligned}-C_1 \sin \beta L - C_2 \cos \beta L \\ + C_3 \sinh \beta L + C_4 \cosh \beta L = 0\end{aligned} \qquad (9)$$

The no moment boundary condition implies that

$$w'''(L) = 0$$

$$\begin{aligned}-C_1 \cos \beta L - C_2 \cos \beta L \\ + C_3 \sinh \beta L + C_4 \cosh \beta L = 0\end{aligned} \qquad (10)$$

Using 7 and 8 and writing 9 and 10 in matrix form,

$$[A]\mathbf{C} = \mathbf{0}$$

where $\mathbf{C}$ is $\begin{bmatrix} C_1 \\ C_2 \end{bmatrix}$ and $[A]$ is as follows

$$\begin{bmatrix} \sinh(\beta L) - \sin(\beta L) & \cosh(\beta L) - \cos(\beta L) \\ \cosh(\beta L) - \cos(\beta L) & \sin(\beta L) + \sinh(\beta L) \end{bmatrix}$$

For a non trivial solution, the determinant of the matrix must be zero.

This leads to the following transcendental equation:

$$\cosh(\beta L) \cos(\beta L) = 1 \qquad (11)$$

Solving this transcendental equation yields values of $\beta_i L$ or the normalized frequencies, which can then be plugged back into equation 6 to get mode shapes defined by the following equation:

$$\begin{aligned} w_n(x) = & \sinh \beta_n x + \sin \beta_n x + \\ & \frac{\sin \beta_n L - \sinh \beta_n L}{\cosh \beta_n L - \cos \beta_n L}[\cosh \beta_n x + \cos \beta_n x] \end{aligned} \qquad (12)$$

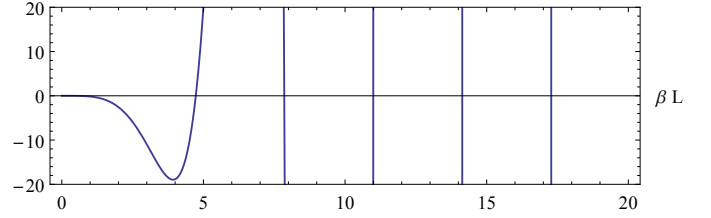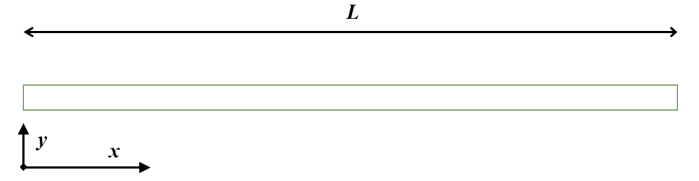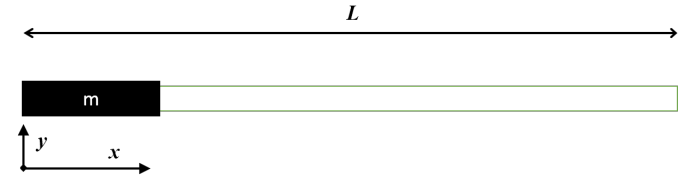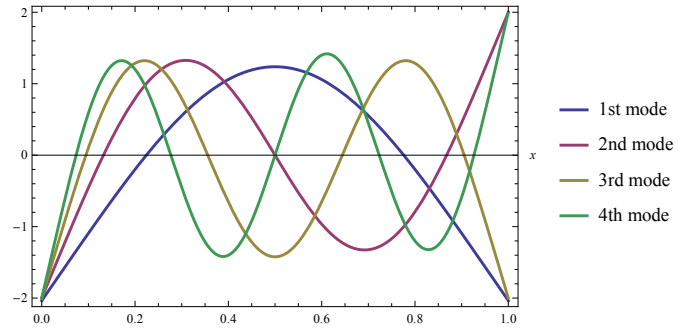The shapes described in equation 12 can be seen graphically in Figure 7c.

Fig. 6. Plot of Equation 19 to evaluate the roots βL. The transcendental function is plotted on the y-axis.
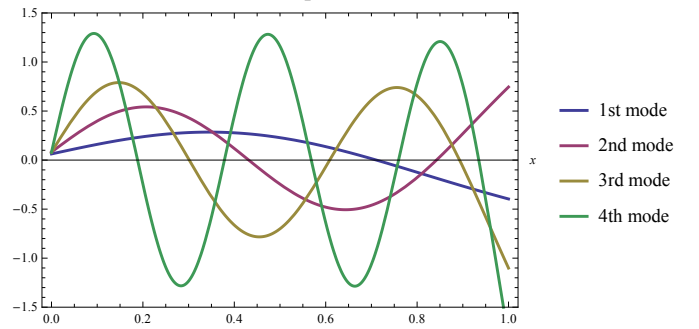

(a) Uniform Density Free Free Beam Model

(b) Free-free beam with point mass addition model of rocket

(c) First four Mode Shapes for a Free-Free Beam Model

(d) First four mode shapes of free free beam with point mass addition

Fig. 7. Analytical results of a free-free beam and free-free with mass beam, where a–b show the models used, and c–d show the shape of the first four vibrational modes.

C. Point mass free free beam

One limitation of the analytical model discussed above is that it assumes that the mass of the rocket is uniformly distributed. However, in the case of our rocket, the motor and the motor mount make the tail end heavier. In order to model this, we refined the model in the previous section to include a point mass in the left end of the beam – as shown in Figure 7b.

The governing equation for this system, the expression for resonant frequencies and the spatial component function of the standing wave solution may be written in the same way as in the previous section (refer to equations 2, 3 and 4).

This model however, has different boundary conditions. These boundary conditions are applied as follows:

Applying the no-moment boundary condition on the left end

$$y''(0) = 0$$

$$\implies C_3 = C_1 \tag{13}$$

Let us assume that the temporal function in Equation 3 is given by

$$u(t) = A\cos\omega t \tag{14}$$

where A is an arbitrary constant and ω is the natural frequency of the beam. Applying the shear boundary

TABLE I.   MODE NUMBER AND FREQUENCIES (HZ)

Mode #	Normalized freq.	Resonant freq.	Uncertainty
0	0	0	0
1	4.04183	36.84363	11.42561
2	7.13384	114.7765	35.59344
3	10.2556	237.2538	73.57496
4	13.3878	404.2265	125.355
5	16.5227	615.6989	190.9349
6	19.6598	871.695	270.322
7	22.798	1172.195	363.5103
8	25.937	1517.211	470.5033
9	29.0766	1906.749	591.3035

TABLE II.   RELAVANT ROCKET SPECIFIC PARAMETERS AND THEIR VALUES

Parameter	Value	Uncertainty
r_{in}	4.56 cm	0.2 cm
r_{out}	4.56 cm	0.2 cm
A	5.259708 cm^2	0.226224 cm^2
E	3 GPa	500 MPa
ρ	156 kg/m^3	25 kg/m^3
L	1.44 m	0.1 m
I	56.88532 m^4	8.188907 m^4

condition on the left side of the beam:

$$EI\frac{\partial^3 y}{\partial x^3} = -m\frac{\partial^2 y}{\partial t^2}$$

Substituting $y(x,t) = w(x)u(t)$,

$$EI\frac{\partial^3 w(x)u(t)}{\partial x^3} = -m\frac{\partial^2 w(x)u(t)}{\partial t^2}$$

$$\implies EI\beta^3(C_4 - C_2) - 2mC_1\omega^2 = 0 \tag{15}$$

Now that we have applied boundary conditions on the left side of the beam, we will apply boundary conditions to the right end of the beam.

Since the right side is free and has no point mass addition, we apply the no moment and no shear boundary conditions.

$$\left.\frac{\partial^2 w(x)}{\partial x^2}\right|_{x=0} = 0$$

which leads to the following equation:

$$C_1(\cosh\beta L - \cos\beta L) \\ -C_2\sin\beta L + C_4\sin\beta L = 0 \tag{16}$$

The no shear boundary condition implies that at $x = L$

$$\left.\frac{\partial^3 w(x)}{\partial x^3}\right|_{x=L} = 0 \tag{17}$$

$$-C_2\cos\beta L \\ +C_1(\sin\beta L + \sinh\beta L) \\ +C_4\cosh\beta L = 0 \tag{18}$$

Writing Equations 13, 15, 16, 18 in matrix form, we get the following:

$$[A]\mathbf{C} = \mathbf{0}$$

where $\mathbf{C}$ is $\begin{bmatrix} C_1 \\ C_2 \end{bmatrix}$ and $[A]$ is as follows

$$\begin{pmatrix} -1 & 0 & 1 & 0 \\ -2m\omega^2 & -EI\beta^3 & 0 & EI\beta^3 \\ \cosh(L\beta) - \cos(L\beta) & -\sin(L\beta) & 0 & \sinh(L\beta) \\ \sin(L\beta) + \sinh(L\beta) & -\cos(L\beta) & 0 & \cosh(L\beta) \end{pmatrix}$$

But, $m = \alpha\rho L$ and $\omega = (\beta L)^2\sqrt{\frac{EI}{\rho A}}$. This implies that

$$m\omega^2 = \alpha(\beta L)\beta^3 EI$$

Substituting this expression for $m\omega^2$ into [A], reduces [A] to:

$$\begin{pmatrix} -1 & 0 & 1 & 0 \\ -2\text{EI}L\alpha\beta^4 & -\text{EI}\beta^3 & 0 & \text{EI}\beta^3 \\ \cosh(L\beta) - \cos(L\beta) & -\sin(L\beta) & 0 & \sinh(L\beta) \\ \sin(L\beta) + \sinh(L\beta) & -\cos(L\beta) & 0 & \cosh(L\beta) \end{pmatrix}$$

For the non-trivial solution, the determinant of the 4x4 matrix must be equal to zero.

Simplifying the determinant, we get the following transcendental equation:

$$-2\beta^3\text{EI}(\alpha\beta L \cos\beta L \sinh\beta L \\ + \cosh\beta L \cos\beta L - \alpha\beta L \sin\beta L) = 1 \tag{19}$$

The above transcendental equation reduces to equation 11 when the point mass or α is set to 0. The transcendental equation was solved numerically using Mathematica's `FindRoots` command. Since the `FindRoots` command solves for the solution in the region of a provided guess, the guesses were provided according to a graphical plot of the function, shown in Figure 6.

This yielded the normalized frequencies ($\beta_i L$) shown in Table I. These normalized frequencies are independent of the particular characteristics of the rocket. By plugging values of E, I, ρ, L and A into equation 4, we can determine values for the resonant angular frequencies of the rocket. Table II shows the relevant constants and the values used for those constants in order to determine the resonant frequencies of the rocket.

In order to determine the values listed in Table II, we used the following formulas [6]:

$$A = \pi(r_{out}^2 - r_{in}^2)$$
$$I = \frac{1}{4}\pi(r_{out}^4 - r_{in}^4)$$
$$\partial A = 2\pi(r_{out} - r_{in})\partial r$$
$$\partial I = \pi(r_{out}^4 - r_{in}^4)\partial r$$
$$\partial\omega_i = \omega_i\sqrt{\left(\frac{\partial E}{2E}\right)^2 + \left(\frac{\partial I}{2I}\right)^2 + \left(\frac{\partial\rho}{2\rho}\right)^2 + \left(\frac{\partial A}{2A}\right)^2 + \left(\frac{2\partial L}{L}\right)^2}$$

IV. FINITE ELEMENT MODELING OF THE ROCKET

Having developed a simplified analytical model of the rocket, we used SolidWorks to create more complex numerical model, using finite element analysis.

In this section, we discuss the results of a finite element analysis of our rocket model in software. For this purpose, we used SolidWorks' Frequency Analysis feature. The SolidWorks assembly of the rocket included a nosecone made of PP homopolymer material. The rest of the body was made using balsa wood. We

(a) 1st mode at 28.319 Hz (b) 2nd mode at 106.37 Hz

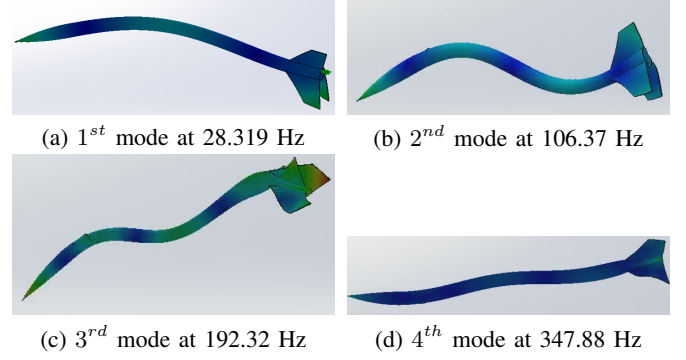(c) 3rd mode at 192.32 Hz (d) 4th mode at 347.88 Hz

Fig. 8. First four Mode Shapes obtained from FEM Analysis

would have used the corrugated paper material available in SolidWorks, but corrugated paper has a non-linear stress-strain curve (non-isotropic material). Thus it does not have a constant Young's modulus of elasticity, which is necessary for a SolidWorks finite element analysis. Therefore, we used balsa wood — which has material properties similar to those of corrugated paper — as the rocket material.

The results of this model are shown in Figure 8.

V. FLIGHT MODEL SIMULATION OF THE ROCKET

In order to determine the velocities which the rocket reaches, we ran an OpenRocket simulation with our Barracuda rocket. After updating the stock ``.ork'' file to include our modifications, we ran simulated flights on both a G79 and an H165 motor. We used these results only as guide for the flights' velocity profile as well as to determine the length of the delay grain when assembling the motors.

VI. GROUND TESTING

Prior to launching the rocket, we performed a range of tests on the rocket to determine what vibrational frequencies, shapes, and damping factors to expect. This section documents the procedure and results of the following tests: a tap test and sweep test for the vibrational modes of the rocket, and a continuous tap test for effective damping.

A. Tap test

A tap test can help determine the natural vibrational modes of the rocket by analyzing the frequency response to a hammer impulse. We performed the tap test with two methods. The first method was to attach a small accelerometer to the rocket body at an arbitrarily chosen location, then tap the rocket with a hammer to excite all the resonant modes. From the frequency response, we determined that the interesting frequencies are in the range of 20 Hz–600 Hz.
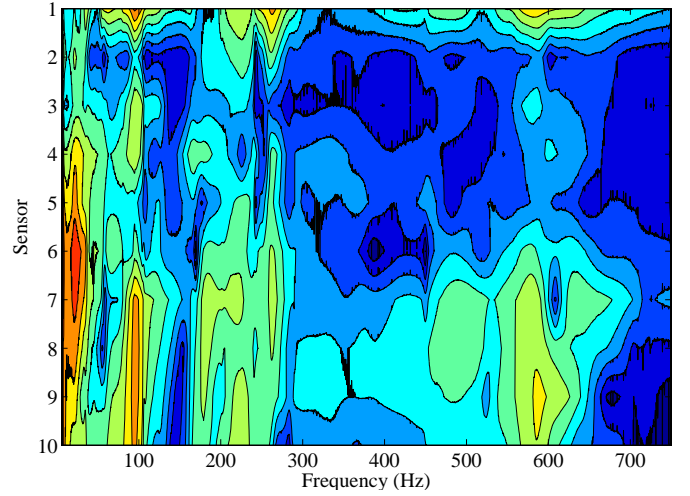
For the second method, instead of using an accelerometer, we recorded the output of the strain gauge array. The benefits of this method was to capture resonant frequencies as well as the shape of each vibrational mode.

We wanted to make a bode plot of the frequency response of our rocket. The development of this bode plot relies on all frequencies in the range of interest to be excited with equal amplitude. This is possible to attain with a tap test if and only if the tap is a perfect impulse that can be approximated as a dirac-delta function. Since our hammer taps are not perfect impulses, we wanted to employ a more sophisticated experimental procedure to excite all frequencies and develop a bode plot of the rocket's frequency response. Hence, we resorted to the sweep test.
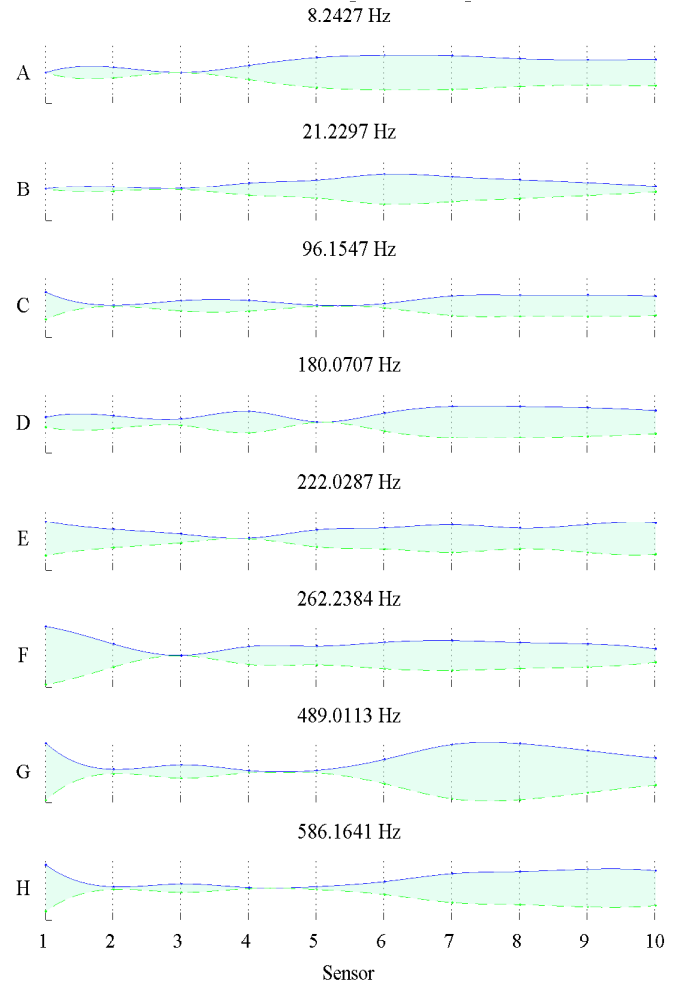
B. Sweep test

In a sweep test, the rocket is continuously excited by a vibrating shake-table. The shake-table vibrations cover a range of frequencies, and the ratio of the sensor output amplitude and vibrational input can be used to analyze the frequency response.

The motor was excited by the shake table from the base of the rocket. In flight, the bottom of the rocket is not attached to anything, but the rocket on the shake table is attached. Since the bottom of the rocket is being excited, the rocket is no longer a free-free beam as assumed in the analytical model. However, even if the bottom is not *free*, it is not fixed either, instead it has a prescribed motion. This is close enough to being a free end [7].

(a) Spatial variation in frequency response. Color corresponds to intensity of vibrations, red being the most intense.

(b) Mode shape of apparent resonant frequencies

Fig. 9. The results of a sweep test with a vibrating table mounted to the rocket motor retainer. Several frequencies showed signs of resonance as illustrated by the red and orange colors in plot (a). The mode shape of those frequencies are plotted in (b). The sensors are numbered and evenly spaced from the nose to the fins of the rocket.

We performed a sweep test from 1 Hz to 750 Hz on the rocket. The RMS output of each sensor determines the response of the section to each frequency.

Figure 9 shows the results of the sweep test on the body of the rocket at all 10 collinear strain gauges. Each sensor has a different response to the range of frequencies, and those differences can be seen in 9a.

Further analysis of the sweep test is discussed in Section .

C. Rocket tube damping

Note: Custom Rocket – In addition to finding the vibrational modes, we sought to determine whether the damping factor is affected by the flight of the rocket. The material of the rocket is underdamped, so we can use the log-decrement method to determine the damping factor.

To monitor the damping in the rocket, we designed an automated tapper device that provides an impulse to the rocket up to 15 times a second. Each tap will give us a transient response, from which we can apply log-decrement in the time domain to find the damping factor of the underdamped system. Given successive peaks' amplitudes A_{t_0} and A_{t_1}, we can find ζ by

$$\zeta = \frac{1}{\sqrt{1 + \left(\frac{2\pi}{\ln(A_{t_0}/A_{t_1})}\right)^2}} \quad (20)$$

Since there are lots of frequencies being excited, we need to filter out all but a particular frequency before performing the log-decrement analysis. A software-based Butterworth bandpass filter of order 3 was used to find a frequency for which the peaks closely aligned with the initial impulse.

Figure 11a-b shows an example of a transient that was passed through a bandpass filtered to extract a frequency. The peaks of the filtered transient is marked by the triangles.

D. Fin damping

The damping of fin vibrations was determined by log-decrement on a impulse transient. Since the fin is fixed on one side, it is a cantilever structure, so the damping factor can be readily obtained. The damping factor of a fin stationary fin was determined to be $\zeta = 0.020 \pm 0.005$ at $385\,\mathrm{Hz}$.

E. Wind tunnel experiment

We measured the structural damping of the rocket at varying velocities in the Harvey Mudd College Wind Tunnel. The maximum wind speeds achieved in the wind
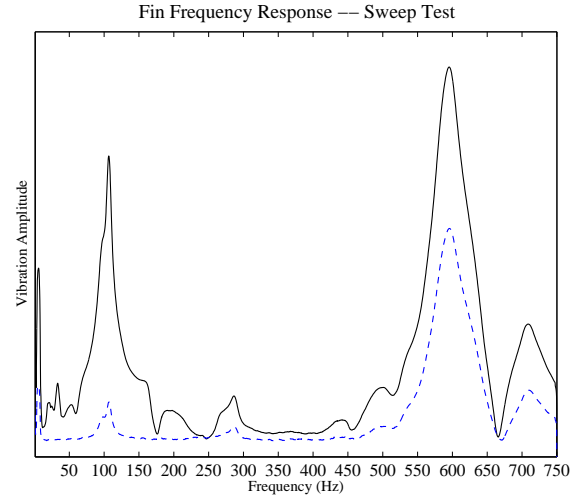

Fig. 10. The frequency response of two sensors on the fin. The amplitude is the natural log of the rms of each sensor. The solid line is the sensor furtherest from the rocket, and the dotted line is closest.
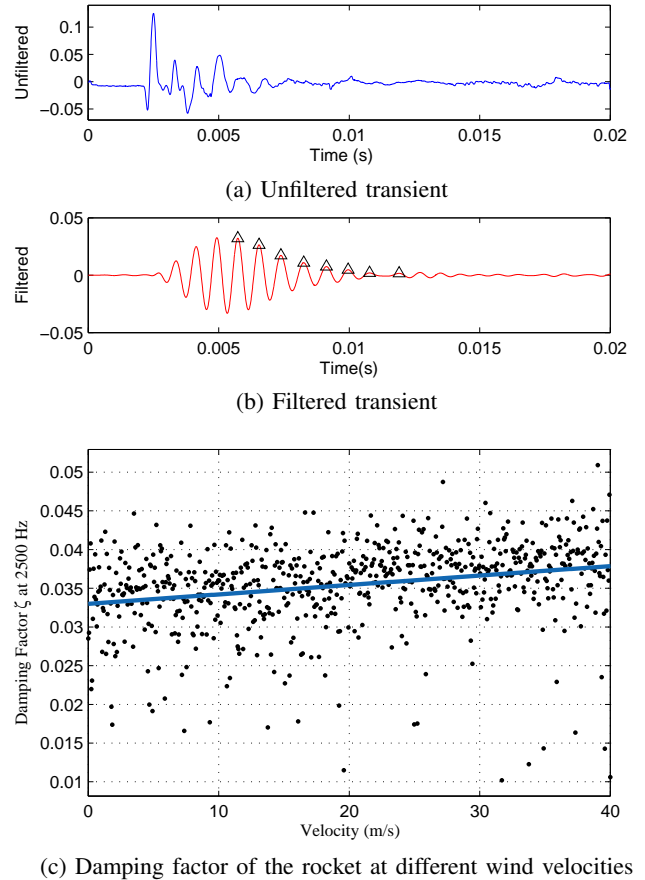

(a) Unfiltered transient

(b) Filtered transient

(c) Damping factor of the rocket at different wind velocities

Fig. 11. Wind velocity has a slight effect on the structural damping of the rocket. The vibrational transient of each tap (a) is filtered at $2500\,\mathrm{Hz}$, and the decaying peaks of the filtered signal (b) is used to calculate the damping factor ζ. The damping factor appears to have a slight positive relation with wind velocity. The slope of the line is $1.22 \times 10^{-4} \pm 0.35 \times 10^{-4}\,\mathrm{s/m}$ within 95% confidence interval.

tunnel is significantly less than the velocities the rocket will undergo during flight. Our rocket is expected to achieve 1.4 mach (476 m/s) whereas the HMC wind tunnel only reaches a maximum of 50 m/s. Hence, we will not be able to fully predict what will happen in flight.

To eliminate external damping factors, no clamps or tape were used to mount the rocket in the wind tunnel. Instead, the rocket was hung on two free-moving suspending supports. The entire rocket was too large to fit in the wind tunnel, so only the payload section was utilized. The automated tapper was set to tap at 8 times a second. The velocity of the wind was estimated by the fan RPM, and the RPM was assumed to be throttled linearly.

The goal of this experiment is not to seek the exact relation between velocity and damping, but instead try to see if velocity of the rocket can affect its damping factor. Hence, the true velocity is not as crucial as the trend of increasing velocity.

From Figure 11c, we can notice a positive correlation between the damping factor and wind velocity. Over a range of 0–40 m/s, the damping factor increases from 0.033 to 0.038. The 95% confidence interval of the positive linear slope is $\pm 0.35 \times 10^{-4}$, which corresponds to a $\pm 30\%$ difference. Further investigation at higher velocities would give important insights about this relationship.

VII. Launch Procedure

Having discussed our ground based testing and modeling, we now move to discussing our flight procedure, from the overall design to the specifics of rocket preparation and launching.

A. Flight Goals

Our experimental goal was to observe which vibrational modes of the rocket were excited during flight. Thus, our goal for each flight the same: to obtain data from the piezoelectric strain sensors on the rocket during its flight.

B. Rocket Preparation

To ensure this data could be collected in safe and repeatable manner, we followed the following procedure to prepare the rocket for flight. Prior to the launch day, we assembled the rocket motor, taking care to trim the delay charge to eject at a time in accordance with the predicted apogee time. On launch day, we assembled the rocket, ensuring all the sensor wires running along the rocket were connected and secured onto the rocket body with tape. Next, we inserted the SD card into the datalogger, and secured it in the slot such that when the pressure from the tape was released, the SD card would click back to its in position. This prevents the SD card from being ejected during flight. Just before setting up the rocket on the launch pad, we started the data collection on the logger, inserted into the payload section, and plugged in the piezoelectric sensor cables. Next, we inserted the pnut altimeter into the nose cose, securing it with tape, and finally secured the nose cone on the rocket. Lastly, we inserted the ignition charge into the rocket motor, and attached it to the ignition wires. At this point, the rocket was ready to launch.

C. Flight

We launched the rocket following standard rocket launch procedure, remaining at a safe distance. Our rocket did not have a GPS transmitter on it, so we made sure to carefully watch the rocket during descent. Upon seeing it hit the ground, we walked toward the landing point and retrieved the rocket. Immediately upon finding the rocket, we took out the data logger and stopped the logging process. Upon reaching our launch site, we promptly copied the data file from the SD card to our computer. We also copied the altimeter data to our computer using the USB cable and the PerfectFlite DataCap software.

We were able to launch the rocket twice - first with a G79 motor and then with an H165 motor.

On the H165 flight, the SD card became disengaged from its holder at some point between closing the rocket and reopening it post-flight. This kept the datalogger from completing the data files header, and so we were unable to retrieve the flight data for that launch.

VIII.   DATA ANALYSIS

As mentioned earlier, we were only able to get data from one flight. We chose to analyze this data from just after motor ignition to just before parachute ejection. This region could be identified in the data from the accelerometer results as well as large impulses seen in the vibration data. After parachute ejection, vibrations had much lower amplitude. Furthermore, the sensors on the lower half of the rocket detached from the circuit board upon parachute ejection. For this reason, data after the parachute deployment was not analyzed.

The 8th strain gauge was not functional during flight. To allow for better visualizations of the shape, we interpolated the values for this sensor from the values of the 7th and 9th sensors, both of which were functional.
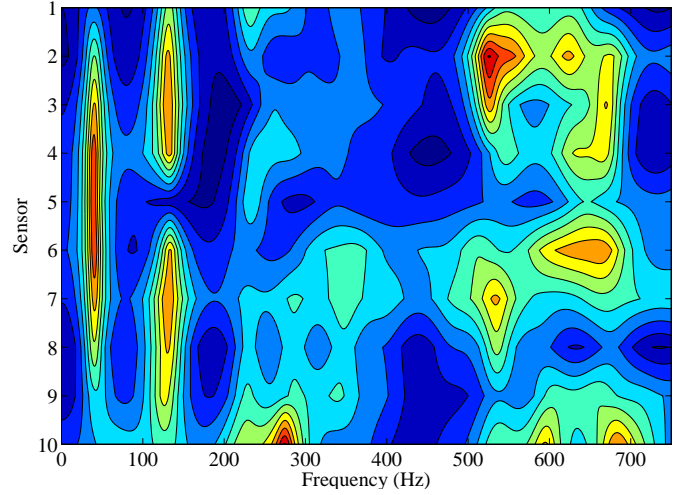
We observed this data in the frequency domain, since for our experimental goal of determining which vibration modes were excited during flight, the frequency data was most relevant. From our models, we knew not to expect resonant modes below 5 Hz, so we filtered the data with a 5th-order Butterworth high-pass filter with a cutoff at 5Hz to focus our analysis on the frequencies we were most interested in. After filtering, we used the Burg method of power spectral density approximation via MATLAB's `pburg` command to obtain polynomial PSD estimates for all the strain gauges. Using this data, were were able to analyze the vibrations of both the rocket body and the fins.
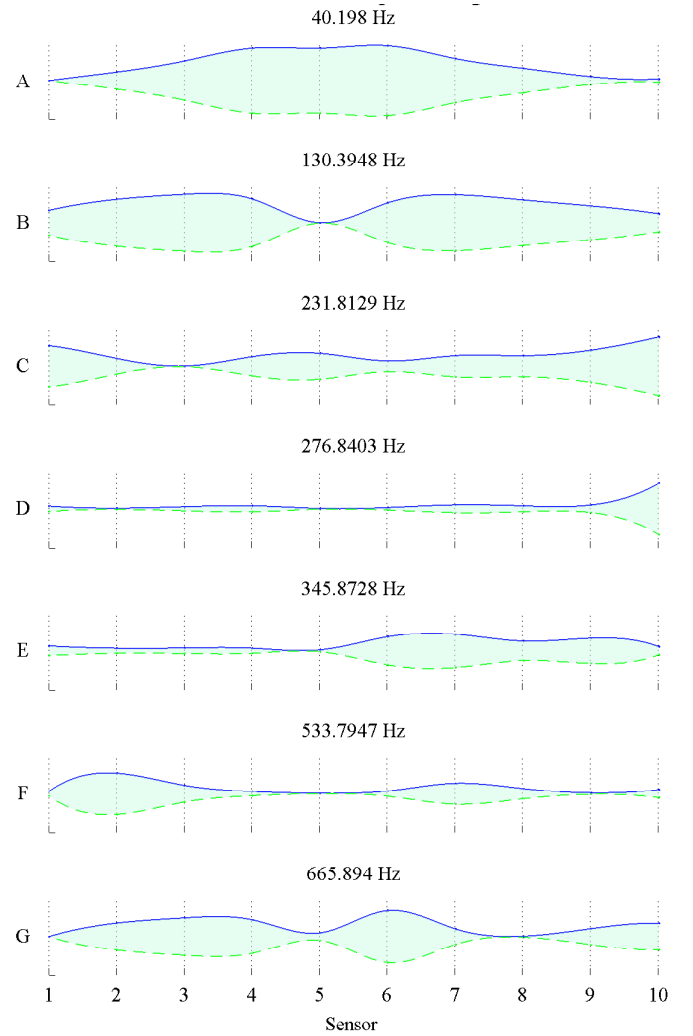
A. Rocket Body Vibrations

1) Results: To visualize the vibration of the rocket as a function of both frequency and position, we created a 2-dimensional plot with frequency and position axes, using color to denote amplitude of vibration. Figure 12 shows this plot. From this data, we can clearly see resonant regions in red.

For each resonant area, we extracted a numerical frequency by taking the average of the relevant peaks in each of the sensors. While the differences in resonant frequencies might be due to the rocket actually being a multipart system, our models treated the rocket as a single system, so we used the mean as a statistic for comparison. The standard deviation of the frequencies of these peaks was used as a measure of the uncertainty in this statistic. Table III shows these results.

At each of these frequencies, we took a cross section of Figure 12a along the spatial axis to visualize the shape of each resonant mode. These shapes are shown in Figure 12b.

(a) Spatial variation in frequency response.

(b) Mode shape of apparent resonant frequencies.

Fig. 12.   Red and orange segments in (a) indicate excited resonant modes in flight. The shapes of these modes is plotted in (b).

2) Comparison to Models: To get a better understanding of these results as well as to ensure that they were reasonable, we can compare them to the models and ground testing discussed previously. In this section, we will consider each resonant mode of vibration observed in flight and compare it individually to our models and ground tests.

The first observed mode of vibration in flight has a frequency of $40.4 \pm 1.3 \, \text{Hz}$. Our analytical model predicted a frequency of $37 \pm 11 \, \text{Hz}$. Our observed frequency is well within the error bounds of this result. The SolidWorks simulation predicted a fundamental frequency of $28.319 \, \text{Hz}$. This is 8σ from our observed result, but the discrepancy can be attributed to a variety of factors, including:

- Inaccuracy of Elastic Modulus: The chosen modulus of elasticity for the simulation was likely different from that of the paper.
- Simplifications of Model: The SolidWorks model treated the rocket body as a single contiguous piece of balsa wood. The actual rocket had several different coupled components.

The models agree with the model regarding the shape of this mode very well. The SolidWorks model shown in Figure 8 shows nodes just before the nose cone and at the fins, with an antinode in the middle. The analytical model also predicted this same shape, seen in Figure 7. This corresponds to the observed nodes at sensor 1 and 10, and the observed antinode near sensor 5. The sweep test showed the first mode at $8.2427 \, \text{Hz}$, and another similarly shaped mode at $21.2297 \, \text{Hz}$. The latter shape, graph B in Figure 9b, aligns better with observed mode in terms of shape and frequency, but the comparison is far from perfect. These differences can be explained by the fact that the sweep test made the rocket a prescribed-free system rather than the free-free system it is in flight.

The second observed mode of vibration has a frequency of $130.5 \pm 2.4 \, \text{Hz}$. The analytical model predicts the frequency for the second mode to be $115 \pm 36 \, \text{Hz}$. Once again, this agrees well with our observed

frequency. The SolidWorks simulation predicted a second resonant mode at a frequency of $106.37 \, \text{Hz}$. This, like for the first mode, is well below the observed in-flight frequency. The error can be attributed to the same causes as in the first mode. The SolidWorks simulation and Analytical Model both agree well with our observed results in terms of the shape of vibration. The sweep test showed a mode similar to the observed mode at $96.1547 \, \text{Hz}$. This shape, shown as shape C in Figure 9b, is quite different from the observed shape, showing 2 nodes in the middle, while the observed mode had only one node in the middle of the shape. Once again, this is likely because the sweep test modeled a different system geometry than the flight.

All observed resonances beyond the second were insufficiently consistent in shape with those predicted by our models to warrant further comparisons. Most likely, the forces exciting the rocket during flight did not excite the higher frequencies.

Nevertheless, there are several notable features in Figure 12a after the frequency of the second mode. First, there is a distinctly quieter response from $300 \, \text{Hz}$ to $450 \, \text{Hz}$. From $500 \, \text{Hz}$ to $750 \, \text{Hz}$, large resonant peaks reappear. The frequencies and shapes of these peaks do not correspond to any of the predictions from the model, suggesting that these are not transverse vibrational modes of the rocket, but perhaps vibrational modes of components in the rocket. The resonance at $524.7 \, \text{Hz}$, plotted as shape F on Figure 12b, shows a localized region of high amplitude around sensors $1 - 3$. This corresponds to the region of the rocket near the circuit board, and could have arisen from resonant vibrations of the circuitboard. Some of the

TABLE III.   HIGH POWER FREQUENCIES OBSERVED DURING FLIGHT.

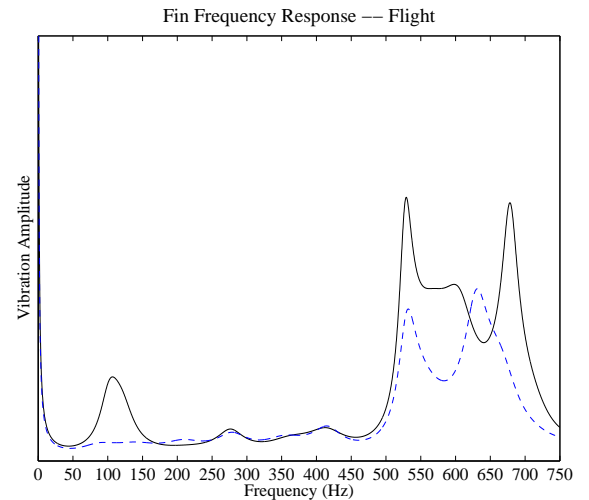| Resonant Frequencies (Hz) |
| --- |
| 40.4 ± 1.3 |
| 130.5 ± 2.4 |
| 232 ± 5 |
| 277 ± 9 |
| 346 ± 9 |
| 534 ± 11 |
| 666 ± 11 |

Fig. 13.   The frequency response measured by both sensors that we placed on one fin of the rocket.

other shapes shown in Figure 12b could be resonant modes in other axes of the rocket — either longitudinal, dilatational, or torsional modes of vibration, modes which our lengthwise positioned strain gauges would not pick up as well.

B. Fin Vibrations

1) Results: The data from the strain gauges on the fin of our rocket were processed the same way as for the sensors on the rocket body. The frequency response of both sensors is shown in Figure 13.

2) Comparison to Models: Ideally, the data collected for fin vibrations during flight should match the data collected with the sweep test — unlike the rocket body, the fin was a fixed-free system in the sweep test as well as in flight. Indeed, when comparing the results seen in Figure 13 to the sweep test results shown in Figure 10, we see that both show a clear peaks near $110\,\mathrm{Hz}$, $280\,\mathrm{Hz}$, and $440\,\mathrm{Hz}$. However, there are discrepancies for the high amplitude peaks near $520\,\mathrm{Hz}$ and $680\,\mathrm{Hz}$. Both of these peaks on the sweep test are approximately $40\,\mathrm{Hz}$ off from the peaks observed in flight. This error could be due to

C. Damping

Due to harsh weather conditions on the scheduled launch date, we were unable to fly our custom rocket and get data regarding damping in flight.

IX. CONCLUSION

The bending vibrations of a rocket are critical to characterize. Knowing how the characteristics of the rockets oscillation change throughout its flight can inform design choices about major stress points, resonant frequencies of various internal components, and possible additional damping. This paper outlined methods to determine such resonant frequencies and resonant mode shapes associated with the rocket.

In order to characterize the rocket system, an analytical model was developed. This analytical model used the Euler-Bernoulli Beam Theory to approximate the rocket as a free-free beam with a point mass attached to one of its ends. This model yielded values for resonant frequencies which fell within one σ of the resonant frequencies obtained from the SolidWorks FEM study, the ground tests (tap test and sweep test) and the final E80 flight. Moreover, the mode shapes describing the transverse bending vibrations of the rocket during flight closely tracked those obtained from the analytical, numerical models.

In addition to the resonant frequencies and the mode shapes, the damping factor of the rocket provides key insight required to accurately describe the bending vibrations of the rocket. In order to complete this characterization, this paper also examined the relation between damping factor and velocity of flight.

In order to find the relation between the effective damping during flight and the velocity of the rocket, an automatic impulse hammer was designed to conduct in-flight tap tests at transonic and supersonic speeds. The log-decrement method was then used in order to process the data and obtain values for the damping factor of the rocket.

It should be highlighted that although many experiments have been conducted to study the pitch-damping of the rocket in transonic and supersonic flight, very few or no experimental studies have been conducted to examine the relationship between the damping associated with the bending vibrations of a rocket and its velocity at transonic and supersonic speeds. Moreover, very few or no experimental studies have employed an automatic impulse hammer to provide clear transients during flight to determine the effective damping of a rocket.

Our experimental results did not perfectly match the predictions of our models. The modal frequencies past the first two did not match as well as the first two. Second, the sweep-test did not prove to be as effective as we had hoped since the shake table forced one end of the rocket to undergo prescribed motion and hence changed the rocket from a free-free system to a prescribed-free system. Third, the analytical model yielded error bars which were 16% of the reported values for natural frequencies. The error bars were so large primarily because of the uncertainty associated with the modulus of elasticity of the non-isotropic material used for the rocket's body. Lastly, not being able to fly our custom rocket to obtain data at transonic and supersonic speeds was a major drawback in our experiment. We hope to obtain this data in the future.

Another potential future direction for this work could be towards experimentally determining the modulus of elasticity of the material in the rocket's body. Yet another direction of improvement would be conduct a sweep test which does not alter the rocket's in-flight characteristic of undergoing free-free motion. One way of doing this would be to use a speaker whose frequency of vibration could be varied over the frequency range of interest.

REFERENCES

[1] Chris Cotner, "Building the Aerotech Barracuda for HMC E80," *Instructables*,
     http://www.instructables.com/id/Building-the-Aerotech-Barracuda-for-HMC-E80/,
     date accessed, May 5, 2014.

[2] "3rd Order Sallen-Key Low-pass Filter Design Tool," *OKAWA Electric Design*,
     http://sim.okawa-denshi.jp/en/Sallenkey3Lowkeisan.htm,
     date accessed, May 5, 2014.

[3] Carlos Felippa, "The Bernoulli-Euler Beam," *Advanced Variational Methods in Mechanics*,
     http://www.colorado.edu/engineering/CAS/courses.d/AVMM.d/AVMM.Ch08.d/AVMM.Ch08.pdf,
     date accessed, May 5, 2014.

[4] David Morin, "The Lagrangian Method," *Introduction to Classical Mechanics*,
     http://www.people.fas.harvard.edu/ djmorin/chap6.pdf,
     date accessed, May 5, 2014.

[5] P. Cha, *Private Communications*, April 8, 2014.

[6] "Modal Vibrations in Rockets," *Harvey Mudd College Engineering*,
     http://www.eng.hmc.edu/NewE80/DynamicBeamLab.html,
     date accessed, May 5, 2014.

[7] Z. Duron, *Private Communications*, April 18, 2014.